Proceedings of the ASME 2010 3rd Joint US-European Fluids Engineering Summer Meeting and 8th International Conference on Nanochannels, Microchannels, and Minichannels
FEDSM-ICNMM2010
August 1-5, 2010, Montreal, Canada

FEDSM-ICNMM2010-30270

COMPUTATIONAL STUDY OF AERIAL SPRAYS USED FOR FOREST PROTECTION

Sydney D. Ryan
Department of Mechanical Engineering
University of New Brunswick
Fredericton, New Brunswick E3B 5A3
Canada
Email: t939a@unb.ca

Andrew G. Gerber*
Department of Mechanical Engineering
University of New Brunswick
Fredericton, New Brunswick E3B 5A3
Canada
Email: agerber@unb.ca

Gorden A. L. Holloway
Department of Mechanical Engineering
University of New Brunswick
Fredericton, New Brunswick E3B 5A3
Canada
Email: holloway@unb.ca

Ali Bagherpour
Department of Mechanical Engineering
University of New Brunswick
Fredericton, New Brunswick E3B 5A3
Canada
Email: t2elf@unb.ca

ABSTRACT

The efficacy of pesticide sprays is strongly dependent on the accuracy of the droplet size spectrum. Over estimates of droplet size may result in excessive drift or ineffective doses, while under estimates of droplet size result in excessive releases. This situation is not only bad for the environment; it incurs large operating costs (spray usually accounts for 30% of total cost). This paper describes the study of droplet sprays commonly used in the agriculture and forestry management. It combines experimental wind tunnel testing and Computational Fluid Dynamic (CFD) methods to develop a fundamental understanding of droplet generation and dispersion in the wake of the atomizer spray system. The results will assist designers of spray technology and applicators in delivering pesticide to its target. The CFD models that are developed and calibrated will further allow the wind tunnel data to be generalized; thus, allowing less wind tunnel testing and eventually direct simulation of droplet dispersion in aircraft wakes.

The CFD models are developed for the poly-dispersed sprays released from a Micronair AU4000 atomizer (a standard atomizer used for forest protection) at an airspeed of 67 m/s. Simulations are performed using a Lagrangian (droplet phase) - Eulerian (fluid phase) procedure and include droplet drag/body forces and turbulent dispersion of droplets. The Baseline Reynolds Stress Model (BSL RSM) turbulence model is used to compute turbulence levels in the air phase. The CFD simulations include the sprayer and a large portion of the wind tunnel geometry in order to facilitate in validation. The computational results are compared to full scale experimental measurements of pressure, gas phase velocity, droplet velocity, and droplet size spectra measured using Phase Doppler Interferometry (PDI) and Hotwire Anemometry. Measurements are available along radial lines at 0.5, 1, 2 and 4 m downstream of the atomizer.

INTRODUCTION

Forest Protection Limited (FPL) and researchers at the University of New Brunswick are slightly past halfway through a

*Address all correspondence to this author.

comprehensive, five-year, research project involving the droplet characterization of aerial atomization systems. The research project includes the experimental measurements of droplet size and velocity distributions within a wind tunnel, as well as the development of Computational Fluid Dynamic (CFD) models. By obtaining a thorough understanding of aerial atomization through combined experimental and computational research, designers of spray technology and applicators will have a better understanding of effective pesticide delivery. This will have a positive impact on the environment, as well as pesticide delivery operating costs.

The details of the accompanying experimental studies are outlined in a separate publication [1]. In this study, the focus is on the CFD model development. The use of CFD modeling to investigate spray formation, by various means, in airflow is not new. However, examining spray formation in the context of rotary atomizers has had little attention, and even less in the forestry industry.

For example, Huang [2] used CFD to model the multiphase flow within a spray dryer fitted with a rotary disc atomizer. An Eulerian-Lagrangian approach was used to model the two-way coupling between the continuous and dispersed phases. The RNG k-ε turbulence model was used along with including vapor to droplet heat and mass transfer. Also, Domnick [3] used CFD to model an electrostatic spray painting process with high-speed rotary bell atomizers. Again, as in [2], the Eulerian-Lagrangian approach and RNG k-ε turbulence model were employed. In both of these studies, experimental work was used to validate the model predictions for droplet diameters and velocities. Neither of these studies considers the unique features of the rotary atomizer employed in this study, which includes upstream blades, and a rotating gauze mesh for droplet breakup into a high-speed air flow.

Further literature review has concluded that no computational study using CFD on rotary atomizers used for forest protection pesticide application has been conducted. Therefore, in response to the lack of basic computational research, a three-dimensional full scale CFD model of the FPL wind tunnel and Micronair AU4000 atomizer is created. The model is used to reproduce and extend accompanying experimental work [1].

EXPERIMENTAL SYSTEM

Experimental work is conducted at FPL's HJ Irving -JJC Picot Wind Tunnel facility in Burpee, New Brunswick. The wind tunnel test section is 1m in diameter and 5m in length [1]. The wind tunnel is open circuit, and it is powered by a 185kW electric motor allowing it to reach speeds between 40 and 270km/h [1]. The wind tunnel contains an open jet test section within an airtight enclosure. The enclosure is transparent allowing for visualization and optical measurements within the test gap. Fig. 1 shows a schematic of the wind tunnel. In the test section, upstream of the open jet, is placed a Micronair AU4000 atomizer, a standard used in aerial pesticide applications and is shown in Fig. 2.

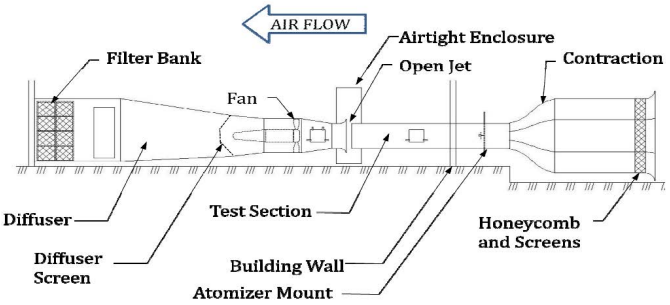

FIGURE 1. WIND TUNNEL SCHEMATIC [1]. Note the airtight (transparent) enclosure and open jet through which measurements are made.

The wind tunnel is equipped with several experimental measuring techniques, namely: a Sympatec Helos Vario laser diffraction system, a 3-component Artium Technologies Phase Doppler Interferometer, hot-wire anemometry, Particle Image Velocimetry (PIV), and high-speed stroboscopic imaging [1]. Data produced by these experimental techniques will be used to develop and validate the computational model. The validated computational model will provide additional detail about the two-phase flow field that cannot be reached experimentally. Furthermore, it can be used to consider conditions outside of the wind tunnel environment. More detail on the experiments used in the validation will be presented with the discussion on the CFD results.

CFD MODEL

A three-dimensional full scale model of the wind tunnel has been created which includes the contraction, the constant diameter test section, the open jet and airtight enclosure, the flow catcher and the primary diffuser. The model was created using NX 6 and is shown in Fig. 3A. Also, a three dimensional model of the Micronair AU4000 atomizer (based on a disk theory approximation) has been created and is shown in Fig. 3B.

In Fig. 3 (top figure), one can see that the open jet and flow catcher are modeled within the enclosure. The contraction profiles, area ratios and lengths of the contractions are identical to the actual wind tunnel. However, the actual cross section of the contraction merges from being hexagonal to circular, whereas the modeled contraction's cross section remains circular. The reason

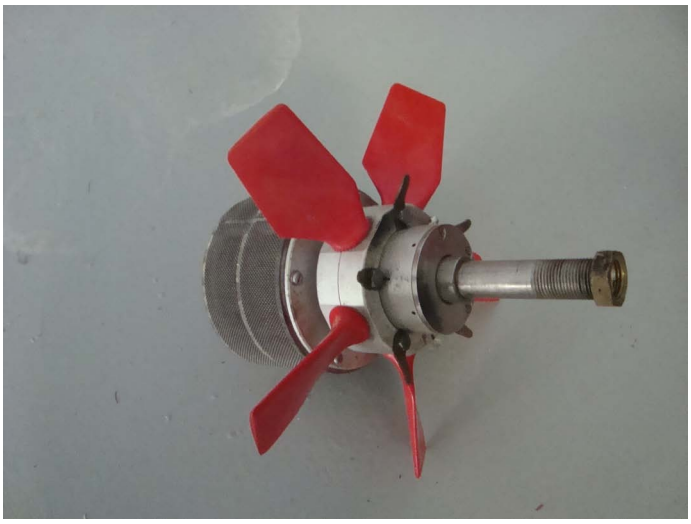

FIGURE 2. MICRONAIR AU4000 ATOMIZER.

for this simplification is to eliminate undesired mesh refinement around this complicated shape merger, and ultimately reduce the computing costs. Later validation against wind tunnel data has shown this approximation to be of little consequence. The atomizer geometry has been simplified to its essential surfaces, and the atomizer blades are not modeled since disc theory will be used to incorporate their effect (and will be elaborated on subsequently). The atomizer can be located at various locations within the test section corresponding to the physical locations during experiments. The atomizer walls are given an angular velocity based on wind tunnel speed (which drives the rotors) and manufacturers RPM data for the atomizer.

The wind tunnel and atomizer models were meshed using ANSYS Workbench 12.1. A longitudinal cross section of the mesh is shown in Fig. 4. The wind tunnel mesh is unstructured and contains 1.17 million nodes for these preliminary investigations. The control volume elements are tetrahedral in shape. There exists an inflation layer (using hexahedral elements) along the wind tunnel walls in order to accurately capture the boundary layer development. The mesh is refined around the atomizer and along the path of its wake to more accurately compute the flow in these regions. It should be noted that the mesh in Fig. 4 is coarser than the actual mesh for visual display.

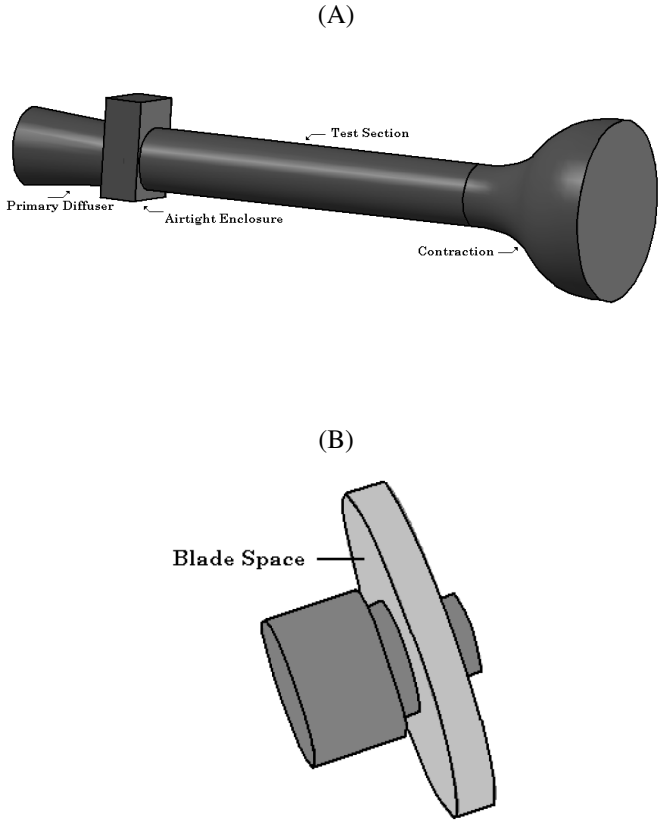

FIGURE 3. (A) WIND TUNNEL MODEL. (B) ATOMIZER MODEL (BASED ON A DISK THEORY APPROXIMATION).

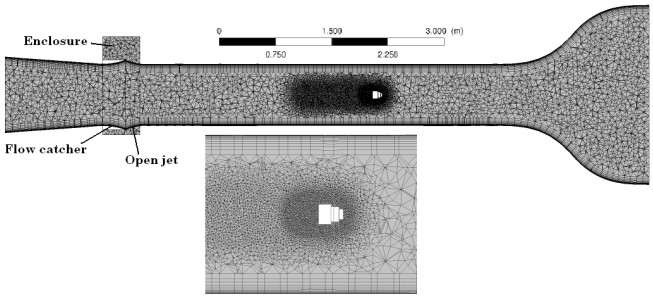

FIGURE 4. WIND TUNNEL MESH.

FLUID MODELS

Gas Phase

The properties of air in all of the CFD simulations are assumed to remain constant and equal to air at 25^o C and 1 atm (see Table 1). The air flow is modeled using an Eulerian frame of reference. During computation, the fluid flow is governed by Eqns. (1-4) which are conservation equations for mass and momentum in all three coordinate directions [4], shown here as:

$$\frac{\partial \rho}{\partial t} + div\left(\rho \vec{U}\right) = 0 \tag{1}$$

TABLE 1. Air Properties at 25^o C and 1 atm [5].

Density, ρ	1.185 kg/m^3
Specific Heat Capacity, c_p	1004.4 J/kgK
Dynamic Viscosity, μ	1.831E-05 $kg/m \cdot s$
Thermal Conductivity, k	0.0261 W/mK

$$\frac{\partial(\rho U)}{\partial t} + div\left(\rho U\vec{U}\right) = -\frac{\partial P}{\partial x} + div(\mu \cdot gradU) + \left[-\frac{\partial\left(\rho\overline{u'^2}\right)}{\partial x} - \frac{\partial\left(\rho\overline{u'v'}\right)}{\partial y} - \frac{\partial\left(\rho\overline{u'w'}\right)}{\partial z}\right] + S_{Mx} \quad (2)$$

$$\frac{\partial(\rho V)}{\partial t} + div\left(\rho V\vec{U}\right) = -\frac{\partial P}{\partial y} + div(\mu \cdot gradV) + \left[-\frac{\partial\left(\rho\overline{u'v'}\right)}{\partial x} - \frac{\partial\left(\rho\overline{v'^2}\right)}{\partial y} - \frac{\partial\left(\rho\overline{v'w'}\right)}{\partial z}\right] + S_{My} \quad (3)$$

$$\frac{\partial(\rho W)}{\partial t} + div\left(\rho W\vec{U}\right) = -\frac{\partial P}{\partial z} + div(\mu \cdot gradW) + \left[-\frac{\partial\left(\rho\overline{u'w'}\right)}{\partial x} - \frac{\partial\left(\rho\overline{v'w'}\right)}{\partial y} - \frac{\partial\left(\rho\overline{w'^2}\right)}{\partial z}\right] + S_{Mz} \quad (4)$$

The form of Eqns. (1-4) is obtained by a Reynolds averaging process in order to incorporate the influence of turbulent unsteadiness. The two terms on the left-hand-side of these equations represent the temporal acceleration and convective terms, respectively. The first term on the right-hand-side represents the pressure gradient followed by the diffusion of momentum. The last two terms represent the Reynolds stresses arising from turbulence and source terms, respectively.

The Reynolds stress terms in Eqns. (2-4) are modeled using the Baseline Reynolds Stress Model (BSL RSM). The BSL RSM is a six-equation turbulence model which improves accuracy when the flow is complex and anisotropic [6]. In order to treat the anisotropy of the turbulence, Reynolds stresses are computed individually for each component. Eqn. (5) shows the modeled equations for Reynolds stresses in tensor form:

$$\frac{\partial\left(\rho\overline{u_i'u_j'}\right)}{\partial t} + div\left(\rho\vec{U}\overline{u_i'u_j'}\right) = P_{ij} + P_{ij,b} + \Phi_{ij} - \frac{2}{3}\beta'\rho k\omega\delta_{ij} + div\left(\left(\mu + \frac{\mu_t}{\sigma_k}\right) grad\left(\overline{u_i'u_j'}\right)\right) \quad (5)$$

In Eqn. (5), P_{ij} and $P_{ij,b}$ are turbulence production terms, Φ_{ij} is the pressure-strain correlation, and β' is a constant. Also, k is the turbulent kinetic energy, μ_t is the turbulent viscosity and σ_k is the turbulent Prandtl number [6]. Also, ω is the turbulent eddy frequency which is transported throughout the domain using Eqn. (6). For the present calculations, there are no source contributions to Eqn. (5) due to the presence of a second phase: an approximation that will be revisited in future studies.

$$\frac{\partial(\rho\omega)}{\partial t} + div\left(\rho\vec{U}\omega\right) = div\left(\left(\mu + \frac{\mu_t}{\sigma_{\omega 3}}\right) grad(\omega)\right) + (1-F_1)\,2\rho\frac{1}{\sigma_2\omega} grad(k)\, grad(\omega) + \alpha_3\frac{\omega}{k}P_k - \beta_3\rho\omega^2 \quad (6)$$

In Eqn. (6), α_3, β_3, $\sigma_{\omega 3}$, and σ_2 are all constants. P_k represents the production of turbulence. Also, F_1 is a blending function which is a function of wall distance used to for boundary layer treatment.

Liquid Phase

The liquid phase droplets are treated in a Lagrangian frame of reference. The following equation of motion describes the forces that affect the droplet motion [7]:

$$m_P\frac{d\vec{U}_P}{dt} = F_D + F_B + F_P \quad (7)$$

In Eqn. (7), m_P and $\vec{U}_P$ represent the mass and velocity of each droplet, respectively. F_D, F_B, and F_P represent the drag force, body force due to gravity and pressure force, respectively. The drag force is determined using the Schiller Naumann drag model which assumes the droplets are sparsely dispersed, and they are sufficiently small that they can be considered spherical [8]. The drag force is calculated using Eqn. (8):

$$F_D = \frac{1}{2}\rho C_D A\,|U_F - U_P|\,(U_F - U_P) \quad (8)$$

where, ρ is the air density, A is the frontal area of the droplet and C_D is the drag coefficient (based on Schiller- Naumann) of

the droplet. The body force acting on a droplet is computed using the density difference between the air and droplets multiplied by the gravity vector. The pressure force is computed using the pressure gradient surrounding the droplet.

Turbulent dispersion forces are used to disperse the particles from regions of high to low particle densities by turbulent fluctuations [9]. That is, turbulent eddies, along with interface drag, cause particles to randomly spread out. The eddies may be characterized by their fluctuating velocity components, u_i' , a length scale (size), l_e, and a time scale (lifetime), τ_{fl}. The fluctuating fluid velocity is dependent on the turbulent kinetic energy, k, using Eqn. (9):

$$u_i' = \Gamma \left(\frac{2k}{3} \right)^{0.5} \tag{9}$$

where Γ is a normally distributed random number to account for the randomness of turbulence. Note that each component of velocity will be given a different random velocity component. The time and length scale of the local turbulent eddies are found using Eqns. (10, 11):

$$\tau_e = \frac{l_e}{\sqrt{\frac{2k}{3}}} \tag{10}$$

$$l_e = C_\mu^{3/4} \frac{k^{3/2}}{\varepsilon} \tag{11}$$

where, ε and C_μ are the turbulent dissipation and turbulence constant, respectively. The factor $C_\mu^{3/4}$ was chosen to relate the characteristic length scale to the eddy dissipation length [10]. Finally, it is important to note that a droplet will interact with a turbulent eddy for a certain time, defined by either the lifetime of the eddy or the time it takes a droplet to traverse the eddy.

BOUNDARY CONDITIONS

The inlet of the computational domain is located at the entrance of the converger. The velocity of the air at the inlet is set so as to obtain a test section wind tunnel velocity as shown in Table 2. The inlet turbulence intensity used is 8 percent as this gave the best results, in combination with the RSM model, when compared to unobstructed experimental data (to be described in a later section). In these calculations, the inlet turbulence length scale is auto computed. The outlet of the computational domain is located at the exit of the primary diffuser. The average static pressure is defined at the outlet based on experimental measurements. Finally, the walls of the wind tunnel are given a no slip

TABLE 2. CFD Model Parameters.

Wind tunnel velocity	67 m/s
Atomizer Speed	8600 RPM
Inlet turbulence intensity	8%
Liquid flow rate	4 L/min

condition and modeled as rough walls with a sand grain roughness of ∼0.2mm. The air tight enclosure and flow catcher are also modeled as no slip walls. However, the roughness of these components is treated as smooth.

The surfaces of the atomizer are modeled as no slip rough walls. The atomizer walls are given a rotational velocity based on experimental measurements (see Table 2) at different wind tunnel speeds. The outlet of the sprayer (the gauze mesh) injects particles from random locations with a size distribution extracted from experiments (as will be described later). Assuming negligible slip, the droplets are given a tangential velocity equal to the atomizer's tangential velocity. The droplets are also given a radial velocity component based on the volumetric flow rate as given in Table 2.

BLADE DISC

In order to reduce computational costs, the atomizer blade geometry is not included in the CFD model. Instead, a cylindrical disk is used encompassing the swept blade volume, as shown in Fig. 3B. Source terms within the disk are used to remove linear and angular momentum from the air flow. Simple turbine blade analysis is used to estimate the momentum terms added to S_{Mx}, S_{My} and S_{Mz}, in Eqns. (2-4). Fig. 5 shows the cross section of a blade along with the associated axial (F_a) and tangential (F_t) aerodynamic forces.

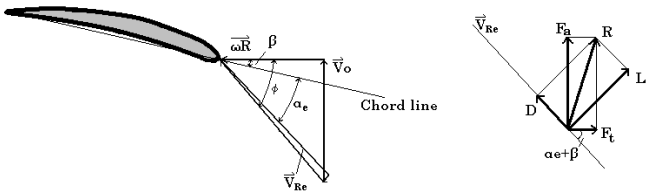

FIGURE 5. BLADE CROSS SECTION WITH VELOCITIES AND FORCES.

In Fig. 5, V_o is the absolute air speed, ωR is the absolute blade velocity and V_{Re} is the absolute effective relative air veloc-

TABLE 3. Blade Properties.

Number of blades	5
Planform area (1 blade), A_p	45 cm^2
C_L	0.35
C_D	0.23
Blade angle, β	35^o

ity after accounting for downwash. Also, β is the blade angle, ϕ is the relative angle between the air speed and blade speed, and α_e is the effective angle of attack of the blade. The forces shown include the lift force, L, and drag force, D, as defined in Eqns. (12,13):

$$L = \frac{1}{2}\rho C_L A_p V_{Re}^2 \times \#blades \tag{12}$$

$$D = \frac{1}{2}\rho C_D A_p V_{Re}^2 \times \#blades \tag{13}$$

Here, A_p is the planform area of one blade and C_L and C_D are approximated lift and drag coefficients of the blades [11]. These values are summarized in Table 3. The lift and drag forces may be transformed into axial and tangential forces by rotating the axis of interest an angle, $\alpha_e + \beta$, as shown in Eqns. (14,15).

$$F_a = L \cdot \cos(\alpha_e + \beta) + D \cdot \sin(\alpha_e + \beta) \tag{14}$$

$$F_t = L \cdot \sin(\alpha_e + \beta) - D \cdot \cos(\alpha_e + \beta) \tag{15}$$

The axial and tangential force components are distributed within the blade space as axial and tangential momentum sinks, respectively. These sources are then further transformed to the x, y, z directions implied by Eqns. (2-4).

RESULTS AND DISCUSSION

Unobstructed Flows

This section focuses on the computational results relating to the unobstructed wind tunnel case (i.e. absence of the atomizer). Pressure measurements, using Pitot tubes, at various wind tunnel locations were performed for several operating speeds. Three of the experimental pressure tap locations were located within the computational domain at: the test section entrance, the test section exit, and the primary diffuser exit. The unobstructed CFD model was run at different wind tunnel speeds to produce curves of pressure versus wind tunnel speed at the three aforementioned locations. Fig. 6 shows the computational results compared to the experimental pressure profiles.

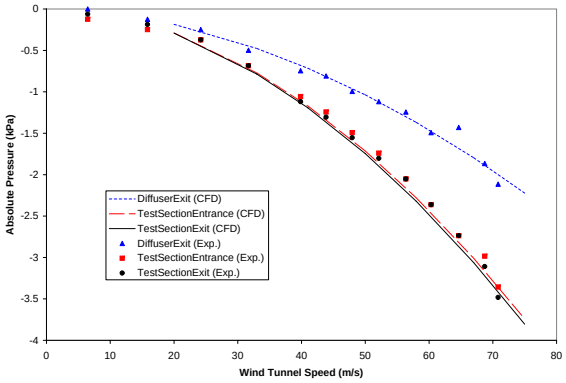

FIGURE 6. COMPUTATIONAL AND EXPERIMENTAL PRESSURE PROFILES.

The CFD results closely follow the experimental trends. The pressure at each wind tunnel location decreases quadratically with increasing wind tunnel speed. Fig. 6 also shows that there is a very small pressure drop across the test section which becomes only slightly noticeable at high wind tunnel speeds.

Hotwire anemometry was also used to experimentally measure the velocity and turbulence intensity profiles just upstream of the test section plane [1]. The measurements were taken at a wind tunnel speed of 67 m/s and without the atomizer in place. The unobstructed CFD model was used to replicate these results which are shown in Fig. 7. The radial velocity (U) is normalized by the centerline velocity (U_c) and the radial position (r) is normalized by the diameter of the atomizer (D).

From Fig. 7 it can be seen that the velocity (as expected for turbulent flow) is nearly constant over the cross section of the wind tunnel except for the boundary layer, which has grown to approximately 10 cm at the test section plane. The turbulence level across the plane is roughly 0.4 %. The CFD and experimental velocity and turbulent intensity profiles match quite well. However, the CFD model slightly under-estimates the turbulence levels within the boundary layer. The unobstructed CFD model,

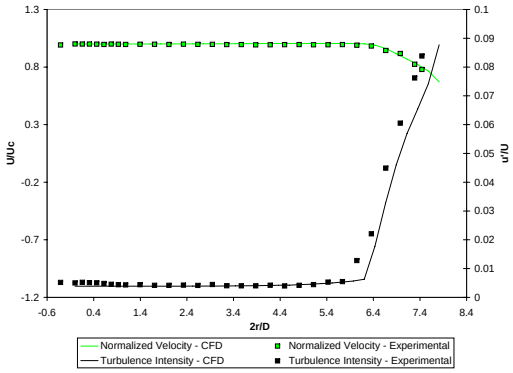

FIGURE 7. COMPUTATIONAL AND EXPERIMENTAL RADIAL PROFILES OF VELOCITY AND TURBULENCE LEVELS, 67m/s WIND TUNNEL SPEED.

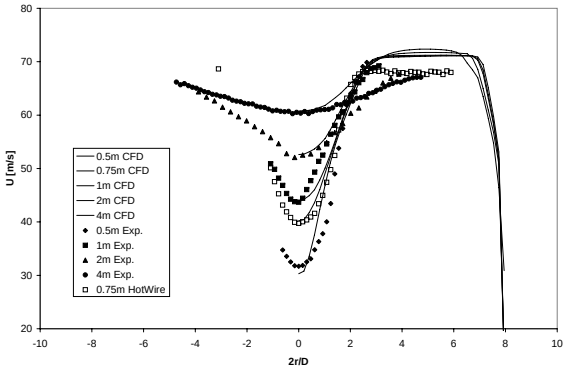

FIGURE 8. COMPUTATIONAL AND EXPERIMENTAL RADIAL PROFILES OF VELOCITY, 67m/s WIND TUNNEL SPEED, 8600RPM ATOMIZER SPEED.

in conjunction with the experimental data in Fig. 6 and 7, was used in determining the appropriate inlet turbulence levels, wall roughness and near wall grid resolutions before moving on to the obstructed flow cases discussed next.

Obstructed Flows

Bagherpour [1] uses Phase Doppler Interferometry and hotwire anemometry to measure the velocity and turbulence intensity profiles at the following downstream positions from the atomizer: 0.5, 0.75, 1, 2 and 4 m. Fig. 8 and 9 show these results plotted against CFD results. The solid lines represent the CFD profiles, the solid symbols and hollow symbols represent the PDI and hotwire data, respectively.

In Fig. 8, it is apparent that the CFD and experimental centerline velocities are very similar for all downstream locations. The CFD simulations do not include 2-way coupling of the air and droplets which may improve the results. In reality, larger droplets do have a significant effect on the gas phase by removing momentum from the air and increasing turbulence levels. Therefore, the CFD results tend to underestimate the size of the wake compared to the PDI results. Not containing droplets, the hotwire measurements match the CFD results more closely.

Fig. 9 shows the turbulence levels at 0.75 m and 4 m for CFD and hotwire measurements. The CFD results generally underestimate the turbulence levels. As mentioned, in the Blade Disk section of the report, momentum source terms were used to simulate the turbine blades. However, turbulence induced by the blades was ignored. By adding turbulent source terms to the blade disk, it is expected that the turbulence levels in the downstream airflow will more closely match the experimental results. Furthermore, the increase in turbulence levels will diffuse the low velocity wake outwards increasing its width. It is expected this will improve the CFD results shown in Fig. 8. However, estimating the appopriate turbulence sources introduced by the blades is necessary and not trivial.

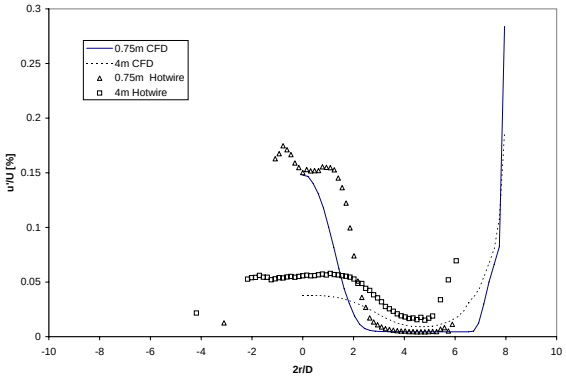

FIGURE 9. COMPUTATIONAL AND EXPERIMENTAL RADIAL PROFILES OF TURBULENCE LEVELS, 67m/s WIND TUNNEL SPEED, 8600RPM ATOMIZER SPEED.

Droplets are injected randomly over the entire guaze face

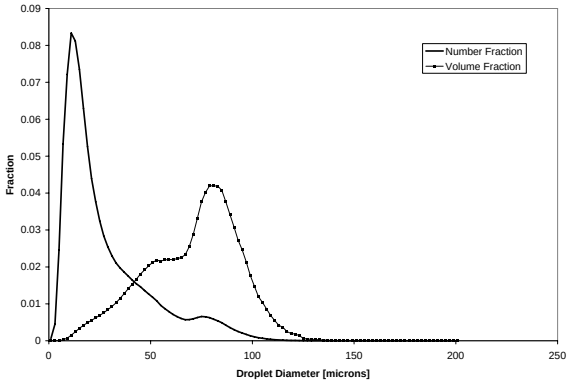

FIGURE 10. DROPLET NUMBER AND VOLUME FRACTION DISTRIBUTIONS APPLIED TO THE SPRAY LEAVING THE ATOMIZER.

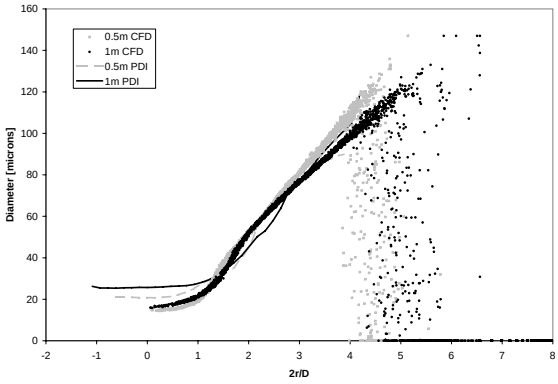

FIGURE 11. COMPUTATIONAL AND EXPERIMENTAL VOLUME AVERAGED MEAN DROPLET DIAMETER (SEE TABLE 2 FOR MODEL PARAMETERS).

of the atomizer with a number and volume fraction distribution corresponding to experimental results at 0.5 m downstream, as shown in Fig. 10. High speed camera observations appear to indicate that significant particle break up occurs both within the atomizer and slightly after exiting the atomizer [1]. Since the CFD simulations do not consider particle breakup at the present time, injecting the particles according the distribution at 0.5 m downstream assumes that all droplet break up has occurred within the atomizer prior to leaving its gauze surface. Once particles leave the atomizer surface, droplet momentum and drag forces act to segregate the droplets according to size. The larger, heavier particles contain more momentum and travel in a radial direction longer before drag forces convert their motion to an axial direction. The smaller particles are not flung as far, and therefore, congregate closer to the center of the wake plume. To demonstrate this effect, Fig. 11 shows the volume averaged mean droplet diameter (d_{30}) plotted against radial position along with PDI results from Bagherpour [1]. It can be seen that the CFD results slightly under estimate the centerline droplet diameters. However, the segregation of droplet sizes across the wind tunnel radius is very similar to experimental findings. Turbulent dispersion acts to randomly disperse droplets of any size. Therefore, the outer edge of the wake, where few droplets are found, contains a scattered distribution of mean droplet sizes.

A significant benefit of CFD simulations is the ability to examine flow data at every point in the domain. Also, color contour plots may be shown at planes of interest in order to clearly visualize physical trends. Taking advantage of this, Fig. 12 shows an air velocity contour along a longitudinal plane, as well as four different downstream cross sectional planes. Velocity vectors are also shown on the cross sectional planes to highlight the swirl in the flow. The wake clearly diminishes with increasing distance from the atomizer. The velocity vectors organize into a swirling motion by 1m and diminish over the next couple of meters. Fig. 13 shows the volume averaged mean particle diameter along a longitudinal plane, as well as four different downstream cross sectional planes. The size segregation occurs before 0.5 m downstream. Turbulent dispersion causes the plume to increase in size. It also causes smaller particles to diffuse outwards and larger particles to diffuse inwards. Thus, turbulent mixing works to smooth the radial size distribution.

Fig. 14 shows the particle tracks of 100 randomly sampled droplets exiting the atomizer and being transported downstream. The particle tracks are colored based on the averaged volume mean particle diameter. One can see that the larger particles are located towards the outside of the plume, whereas the smaller particles are more centralized. However, farther downstream turbulent mixing tends to remove this droplet size segregation. The close up view of the atomizer in Fig. 14 shows the droplets exiting the atomizer virtually tangential. However, drag forces change their path. The air mean flow forces their motion to be axial, and the turbulent eddies force them to randomly disperse.

CONCLUSIONS AND FUTURE WORK

A full scale three-dimensional CFD model has been created of FPL's HJ Irving -JJC Picot wind tunnel fitted with a Micronair AU4000 atomizer. Experimental PDI and hotwire anemometry

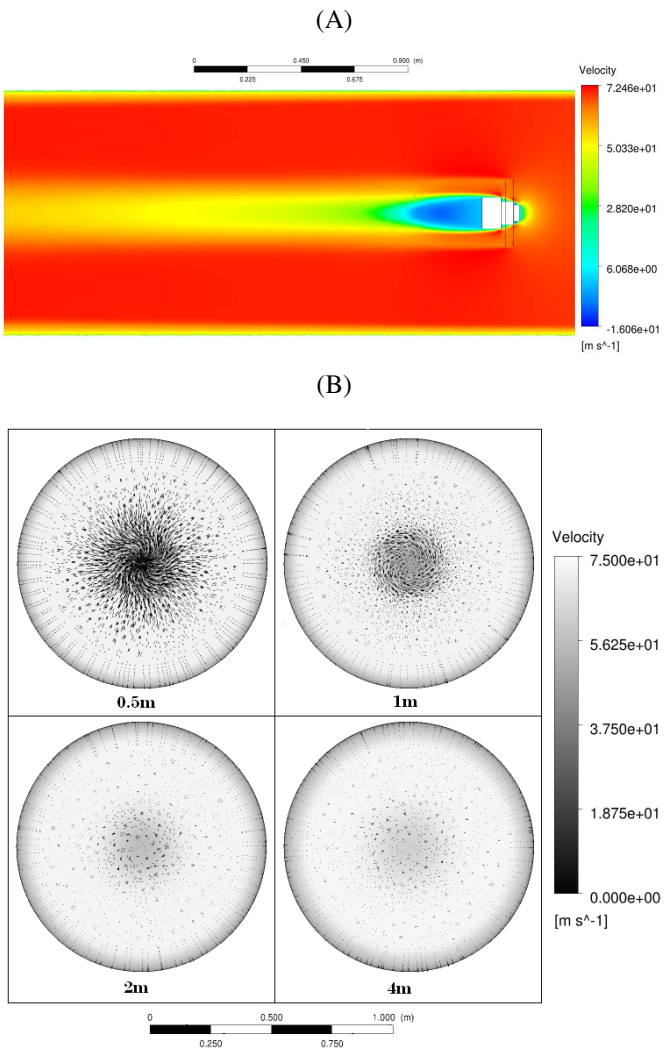

FIGURE 12. (A) AIR VELOCITY ALONG A LONGITUDINAL PLANE. (B) AIR VELOCITY ALONG SEVERAL DOWNSTREAM CROSS SECTIONAL PLANES (SEE TABLE 2 FOR MODEL PARAMETERS).

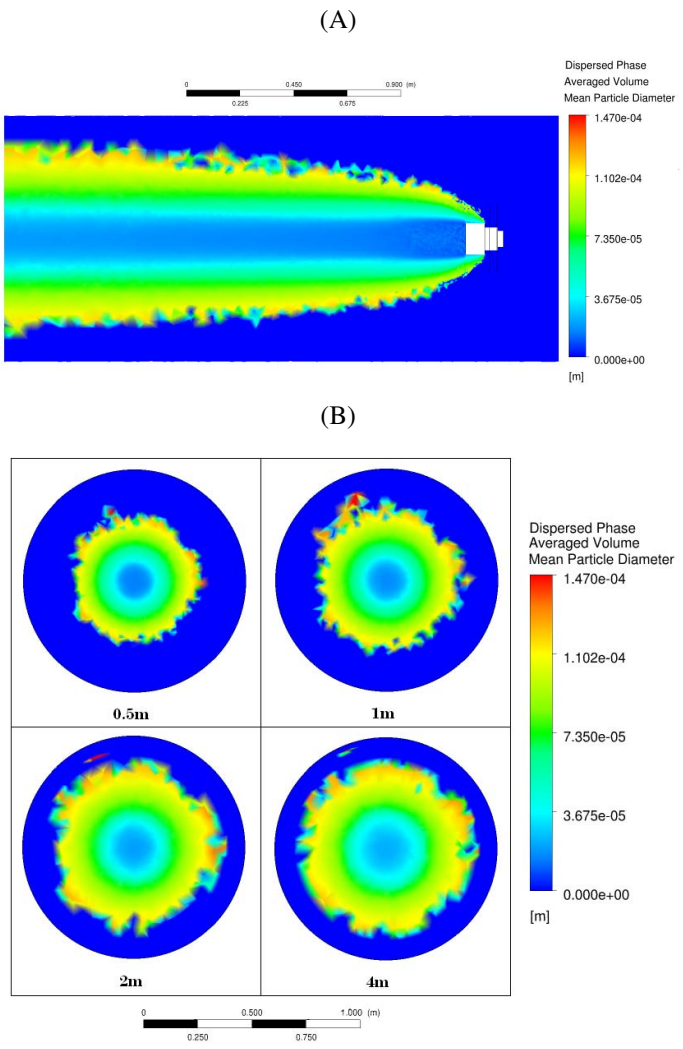

FIGURE 13. (A) VOLUME AVERAGED MEAN PARTICLE DIAMETER ALONG A LONGITUDINAL PLANE. (B) VOLUME AVERAGED MEAN PARTICLE DIAMETER ALONG SEVERAL DOWNSTREAM CROSS SECTIONAL PLANES (SEE TABLE 2 FOR MODEL PARAMETERS).

measurements of Bagherpour [1] are used to validate the computational models. The air is modeled as a continuous Eulerian fluid with constant properties and the droplets in the Lagrangian frame. The turbulence is modeled using the BSL RSM turbulence model. A CFD model of the unobstructed wind tunnel is used to determine proper boundary conditions such as wall roughness and inlet turbulence intensity. With the atomizer included, velocity and turbulence levels at several downstream positions are compared to accompanying experimental data. The centerline velocities match closely to measured values. However, the size of the atomizer's wake tends to be slightly underestimated by the CFD model. The turbulence intensity in the atomizer's wake is also underestimated by the CFD model. This underestimation becomes more pronounced farther downstream. However, the shape of the turbulent intensity profiles are similar to measured data. The average volume mean diameter of the droplets is compared to experimental measurements at various downstream cross sectional planes. The CFD results slightly under estimate the centerline droplet diameters. However, the segregation of droplet sizes across the wind tunnel radius is very similar to experimental findings.

The results obtained at this stage of the research suggest some short and long term work that still needs to be done. In

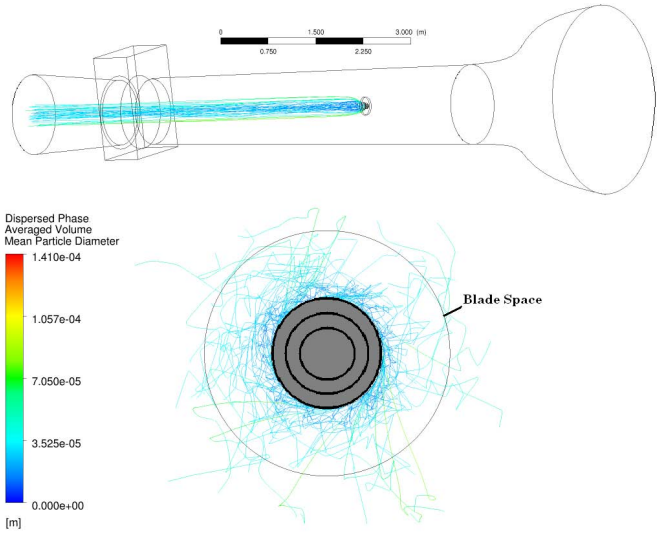

FIGURE 14. PARTICLE TRACKS WITH AVERAGED VOLUME MEAN PARTICLE DIAMETER CONTOUR (SEE TABLE 2 FOR MODEL PARAMETERS).

the near term, the turbulence intensity levels downstream of the atomizer must be investigated in more detail. In this regard, adding turbulent source terms to the blade space should be considered. A further consideration is introducing two-way coupling between the air and droplets. In the longer term, the injected liquid droplets will be studied in greater depth, in particular physical phenomena that occur to droplets as they leave the atomizer and beyond once in the free stream. For example the droplets may experience break up, evaporation, collisions and coalescence which all affect the droplet size distribution and trajectories at downstream measuring stations. These studies will suggest how the droplet volume and number fraction distributions at the atomizer outlet will have to be adjusted to help match experimental downstream data.

ACKNOWLEDGMENT

The author would like to acknowledge the Natural Sciences and Engineering Research Council of Canada (NSERC), Forest Protection Limited (FPL), and the University of New Brunswick (UNB) in funding this research project.

REFERENCES

[1] Bagherpour, A., Holloway, G., and Gerber, A., 2010. "Experimental investigation of aerial spray characteristics". ASME Paper No. FEDSM-ICNMM2010-30707.

[2] Huang, L. X., Passos, M. L., Kumar, K., and Mujumdar, A. S., 2005. "A three-dimensional simulation of a spray dryer fitted with a rotary atomizer". *Drying Technology,* ***23***(9-11), pp. 1859–1873.

[3] Domnick, J., Scheibe, A., and Ye, Q., 2005. "The simulation of the electrostatic spray painting process with high-speed rotary bell atomizers. part i: Direct charging". *Particle and Particle Systems Characterization,* ***23***(5), pp. 408–416.

[4] Versteeg, H. K., and Malalasekera, W., 2007. *An Introduction to Computational Fluid Dynamics: The Finite Volume Method*, 2^{nd} ed. Pearson Education Limited, Harlow, England.

[5] Munson, Y. O., 2006. *Fundamentals of Fluid Mechanics*, 5^{th} ed. John Wiley & Sons, Inc., United States of America.

[6] ANSYS Canada Ltd., 2004. *ANSYS CFX-Solver, Release 10.0: Modelling - Turbulence and Near - Wall Modelling*. ANSYS CFX 10.0 Help Files, pp. 122–129.

[7] Shirolkar, J. S., Coimbra, C. F. M., and McQuay, M. Q., 1996. "Fundamental aspects of modeling turbulent particle dispersion in dilute flows". *Progress Energy Combustion Science,* ***22***, pp. 363–399.

[8] Schiller, L., and Naumann, A., 1933. *VDI Zeits* **77**. pp. 318.

[9] Gosman, A. D., and Loannides, E., 1981. "Aspects of computer simulation of liquid fuelled combustors". *AIAA Journal,* ***81***(0323).

[10] Hinze, J. O., 1975. *Turbulence*. McGraw Hill, New York, U.S.A.

[11] Phillips, W. F., 2004. *Mechanics of Flight*. John Wiley & Sons, Inc., New Jersey, U.S.A.